forests

MDPI

Article

Numerical Study of Focusing Effects of Microwaves inside Wood Due to Timber Ring Structure

Rocio Sanchez-Montero *, Pablo-Luis Lopez-Espi, Juan Antonio Martinez-Rojas, Jesus Alpuente-Hermosilla and Cristina Alen-Cordero

Department of Signal Theory and Communications, Escuela Politecnica Superior, Universidad de Alcala, Campus Universitario, Ctra. de Madrid a Barcelona km 33.600, Alcala de Henares 28805, Spain; pablo.lopez@uah.es (P.-L.L.-E.); juanan.martinez@uah.es (J.A.M.-R.); jesus.alpuente@uah.es (J.A.-H.); cristina.alen@uah.es (C.A.-C.)

* Correspondence: rocio.sanchez@uah.es; Tel.: +34-91-885-6660

Received: 15 January 2018; Accepted: 26 February 2018; Published: 28 February 2018

Abstract: The aim of this study is the detailed calculation of microwave propagation inside raw timber in cylindrical configurations. Two different approaches have been used. The first one uses an exact formulation and analytical approximations in order to explore the electromagnetic field distribution inside dry wood. The introduction of conductivity in the exact model makes it so complex that the equations are unsuitable for analytical manipulation. In order to further explore the effect of moisture in cylindrical wood structures, a full scale numerical simulation using commercial software has been performed. The results show that for microwave frequencies in the 3 GHz range and for typical wood parameters, a cylindrical log behaves as a kind of Fresnel lens. This work has important applications in microwave treatment and sensing of wood.

Keywords: microwave propagation in wood; non-destructive sensing of wood; physical wood treatments; analytical analysis; numerical analysis

1. Introduction

Microwave treatment and sensing of wood is increasingly important. A review of different microwave wood testing techniques is given in [1] and these include propagation modelling, measurement techniques, hardware implementation, and determination of wood properties. According to [2,3], microwave heating, for example, offers several advantages over other drying methods and chemical procedures because its technique is eco-friendlier and causes less damage in the timber sample compared to employing toxic chemicals. Besides, microwave heating method is faster and gentler in comparison to live steam. As a contactless and nondestructive testing technique, microwave scanning is able to estimate several important wood parameters including density, moisture content, and grain angle [4–13]. Following Bucur [14], other non-destructive techniques use X-rays, gamma rays, thermal imaging, ultrasound, nuclear magnetic resonance, and neutron imaging. Microwave based nondestructive techniques have been applied to a variety of applications, including in situ microwave tomography, moisture content determination, anisotropy measurement, online imaging, internal inspection of logs, mechanical grading, and defect detection. Microwaves and ultrasound have similar resolution, but microwaves are not limited by the contact nature of ultrasound transducers.

As far as we know, most models of microwave propagation inside wood are based on rectangular configurations, although some studies in more general geometries are published [15,16]. In [17], the effect of annual growth rings on nondestructive measurements is explicitly studied. This limits the application of microwave techniques in areas such as measurement of living trees in situ.

Important efforts have been made to develop generalized models for water content prediction in wood using its dielectric properties, but detailed models of electromagnetic propagation inside wood

are more modest. Due to the complexity, most models do not consider the effects of the geometry or the dielectric variation and oscillations caused by the ring structure of timber.

This work studies microwave propagation and electric field distribution at 3 GHz inside cylindrical wood structures, following the procedures described in [18–20]. From our previous work [21] with Bragg fibers, it is expected that important focusing effects of microwaves inside wood due to its ring structure may be observed. These focusing phenomena could be very important for the interpretation of testing data and for heating applications, where some zones could be burned while the others would be almost cold. Besides, the quick production of very hot water vapor and volatiles in small areas of the irradiated wood could produce explosions, deformations, and cracks. As microwave heating and treatment of wood is an economical alternative to other methods, it is very important to know the distribution of radiation inside the pieces and the perturbations introduced by the complex structure of this natural material.

Two complementary approaches have been used. First, an exact model based on a complete formulation of the Maxwell equations in cylindrical coordinates has been developed. This model is only analytically tractable in the limit of zero conductivity. This implies that the imaginary part of the wood permittivity is negligible, which is only correct for dry wood. However, some interesting similarities are shared by the dry and moist wood models. This semianalytical model includes the effect of grain angle by means of a correction of the effective permittivity inside wood, avoiding the full use of helicoidal coordinates which produce equations too complex for this case. The resulting equations are then solved by means of an implicit Runge–Kutta (RK), which provides the unconditional stability needed to calculate the values of the corrected permittivity.

The second model uses a full scale numerical simulation of a cylindrical, ring shaped, wood sample. Moreover, the analysis of the influence of the number of rings and the geometry of the rings, by defining unequal rings geometry, in the electric field distribution has been done. The simulations were performed by means of commercial software, CST Microwave Studio® (2017 version, Framingham, MA, USA) [22], which uses finite-integral technique (FIT) algorithms for the computation of the electromagnetic field. Other numerical simulation approaches to the study of microwave propagation in wood can be seen in [23].

Both models agree in the limit of zero conductivity and predict important effects due to the ring structure of cylindrical wood. The results show an important focusing of the radial distribution of the electric field which depends on the number and thickness of the growth rings. Also, stationary wave patterns are observed due to the finite length of wood logs. The important point of this work is to show the effect of the concentric ring structure of wood on the microwave propagation inside timber. This effect is similar to a Bragg fiber, producing interesting focusing phenomena as will be shown.

The rest of the paper is organized as follows: mathematical formulation involving both semianalytical and numerical models is explained in Section 2, then results are presented and discussed in detail in Section 3. Finally, relevant conclusions are presented in Section 4.

2. Mathematical Formulation

2.1. Semianalytical Model

Raw cylindrical timber can be considered a stack of concentrically dielectric layers, so a model with arbitrary periodic variation of dielectric permittivity is the most accurate. Considerable symbolic manipulation of the Maxwell equations in cylindrical coordinates is necessary for arbitrary permittivity functions which can depend only on the radius of the cylinder. The equations for the exact model are derived from our previous works [24,25]. They are reproduced here for completeness.

The equations were obtained as follows. First, we write the complete set of Maxwell equations in cylindrical coordinates

$$\frac{1}{r}\frac{\partial(rD_r)}{\partial r}+\frac{1}{r}\frac{\partial D_\phi}{\partial \phi}+\frac{\partial D_z}{\partial z}=\rho \quad (1)$$

$$\frac{1}{r}\frac{\partial(rB_r)}{\partial r}+\frac{1}{r}\frac{\partial B_\phi}{\partial \phi}+\frac{\partial B_z}{\partial z}=0 \tag{2}$$

$$\frac{1}{r}\frac{\partial E_z}{\partial \phi}-\frac{\partial E_\phi}{\partial \phi}+\frac{\partial B_r}{\partial t}=0 \tag{3}$$

$$\frac{\partial E_r}{\partial z}-\frac{\partial E_z}{\partial r}+\frac{\partial B_\phi}{\partial t}=0 \tag{4}$$

$$\frac{1}{r}\frac{\partial\left(rE_\phi\right)}{\partial r}-\frac{1}{r}\frac{\partial E_r}{\partial \phi}+\frac{\partial B_z}{\partial t}=0 \tag{5}$$

$$\frac{1}{r}\frac{\partial H_z}{\partial \phi}-\frac{\partial H_\phi}{\partial z}-\frac{\partial D_r}{\partial t}-J_r=0 \tag{6}$$

$$\frac{\partial H_r}{\partial z}-\frac{\partial H_z}{\partial r}-\frac{\partial D_\phi}{\partial t}-J_\phi=0 \tag{7}$$

$$\frac{1}{r}\frac{\partial\left(rH_\phi\right)}{\partial r}-\frac{1}{r}\frac{\partial H_r}{\partial \phi}-\frac{\partial D_z}{\partial t}-J_z=0 \tag{8}$$

Performing some algebraic manipulations, the full set of Maxwell equations can be reduced to a pair of coupled ordinary differential equations. The following ansatz is inserted into the cylindrical Maxwell Equations (1)–(8), where r is the radius, z is the length of the wood log, and phi is the angle measured from the radius. E is the electric field strength, H is the magnetic field, D is the electric displacement field, B is the magnetic flux density, omega is the angular frequency, t is the time, and l is the angular moment number.

$$E_{r,\phi,z}=E_{0[r,\phi,z]}e_{r,\phi,z}(r)e^{(il\phi)}\times e^{(i\beta z)}\times e^{-(i\omega t)} \tag{9}$$

$$H_{r,\phi,z}=H_{0[r,\phi,z]}h_{r,\phi,z}(r)e^{(il\phi)}\times e^{(i\beta z)}\times e^{-(i\omega t)} \tag{10}$$

This produces a set of separable equations, assuming $\rho=0$ (charge density) and $J=0$ (current density), which implies that conductivity is not considered. Equations whose terms are in the form βE or βH are selected. These are Equations (1), (2), (4), (6) and (7). Now, the Equations (4), (6) and (7) can be algebraically solved with respect to the radial components $e_r(r)$, $e_\phi(r)$, $h_r(r)$, and $h_\phi(r)$,

$$e_r(r)=-\left(H_{0z}l\mu_0h_z(r)\omega-iE_{0z}\beta r\frac{e_z(r)}{r}\right)\times\left(\varepsilon_0\varepsilon_r(r)\mu_0E_{0r}r\omega^2-E_{0r}\beta^2r\right)^{-1} \tag{11}$$

$$e_\phi(r)=-\left(iH_{0z}\mu_0r\frac{h_z(r)}{r}\omega+E_{0z}l\beta e_z(r)\right)\times\left(\varepsilon_0\varepsilon_r(r)\mu_0E_{0\phi}r\omega^2-E_{0\phi}\beta^2r\right)^{-1} \tag{12}$$

$$h_r(r)=-\left(\varepsilon_0\varepsilon_r(r)E_{0z}le_z(r)\omega+iH_{0z}\beta r\frac{h_z(r)}{r}\right)\times\left(\varepsilon_0\varepsilon_r(r)\mu_0H_{0r}r\omega^2-H_{0r}\beta^2r\right)^{-1} \tag{13}$$

$$h_\phi(r)=\left(\varepsilon_0\varepsilon_r(r)E_{0z}re_z(r)\frac{e_z(r)}{r}\omega-H_{0z}l\beta h_z(r)\right)\times\left(\varepsilon_0\varepsilon_r(r)\mu_0H_{0\phi}r\omega^2-H_{0\phi}\beta^2r\right)^{-1} \tag{14}$$

Substituting this solution into Equations (1) and (2), another pair of ordinary differential equations is obtained. In order to analyze these equations, it is convenient to decoupled them. Using $e_z(r)=e_{zR}(r)+ie_{zI}(r)$; $h_z(r)=h_{zR}(r)+ih_{zI}(r)$ and taking both real and imaginary parts in the resulting equations, the following expressions are finally obtained

$$\begin{gathered}e''_{zR}(r)+A_{11}e'_{zR}(r)+A_{12}e'_{zI}(r)+A_{13}h'_{zR}(r)+A_{14}h'_{zI}(r)+A_{15}e_{zR}(r)+\\A_{16}e_{zI}(r)+A_{17}h_{zR}(r)+A_{18}h_{zI}(r)+A_{19}=0\end{gathered} \tag{15}$$

$$\begin{gathered}e''_{zI}(r)+A_{21}e'_{zR}(r)+A_{22}e'_{zI}(r)+A_{23}h'_{zR}(r)+A_{24}h'_{zI}(r)+A_{25}e_{zR}(r)+A_{26}e_{zI}(r)+\\A_{27}h_{zR}(r)+A_{28}h_{zI}(r)+A_{29}=0\end{gathered} \tag{16}$$

$$h''_{zR}(r) + A_{31}e'_{zR}(r) + A_{32}e'_{zI}(r) + A_{33}h'_{zR}(r) + A_{34}h'_{zI}(r) + A_{35}e_{zR}(r) + A_{36}e_{zI}(r) + A_{37}h_{zR}(r) + A_{38}h_{zI}(r) + A_{39} = 0 \quad (17)$$

$$h''_{zI}(r) + A_{41}e'_{zR}(r) + A_{42}e'_{zI}(r) + A_{43}h'_{zR}(r) + A_{44}h'_{zI}(r) + A_{45}e_{zR}(r) + A_{46}e_{zI}(r) + A_{47}h_{zR}(r) + A_{48}h_{zI}(r) + A_{49} = 0 \quad (18)$$

where A_{ij} (i = 1, 2, 3 and j = 1, ..., 9) coefficients try to simplify the writing of the final equations, because the complete formulae are rather long. These coefficients multiply the radial components, both real and imaginary, of the axial electric and magnetic field inside the cylindrical wood sample.

The value of coefficients A_{ij} defined in the Equation (15) are detailed in the following equations (from Equations (19)–(22))

$$A_{11} = \left(\varepsilon_0\varepsilon_r^2(r)\mu_0\omega^2 - \beta^2 r\varepsilon'_r(r) - \beta^2\varepsilon_r(r)\right) \times \left(\varepsilon_0\varepsilon_r^2(r)\mu_0 r\omega^2 - \beta^2 r\varepsilon_r^2(r)\right)^{-1} \quad (19)$$

$$A_{15} = \left(\varepsilon_0\varepsilon_r(r)\mu_0 r^2\omega^2 - \beta^2 r^2 - l^2\right)r^{-2} \quad (20)$$

$$A_{18} = \left(\varepsilon'_r(r)\mu_0 H_{0z} l\beta\omega\right)\left(\varepsilon_0\varepsilon_r^2(r)\mu_0 E_{0z} r\omega^2 - \varepsilon_r(r) r E_{0z}\beta^2\right)^{-1} \quad (21)$$

and where

$$A_{12} = A_{13} = A_{14} = A_{16} = A_{17} = A_{19} = 0 \quad (22)$$

A_{ij} (i = 2 and j = 1, ..., 9) coefficients employed in the Equation (9) are defined in the Equations (23)–(26)

$$A_{22} = \left(\varepsilon_0\varepsilon_r^2(r)\mu_0\omega^2 - \beta^2 r\varepsilon'_r(r) - \beta^2\varepsilon_r(r)\right) \times \left(\varepsilon_0\varepsilon_r^2(r)\mu_0 r\omega^2 - \beta^2 r\varepsilon_r^2(r)\right)^{-1} \quad (23)$$

$$A_{26} = \left(\varepsilon_0\varepsilon_r(r)\mu_0 r^2\omega^2 - \beta^2 r^2 - l^2\right)r^{-2} \quad (24)$$

$$A_{27} = -\left(\varepsilon'_r(r)\mu_0 H_{0z} l\beta\omega\right)\left(\varepsilon_0\varepsilon_r^2(r)\mu_0 E_{0z} r\omega^2 - \varepsilon_r(r) r E_{0z}\beta^2\right)^{-1} \quad (25)$$

and where,

$$A_{21} = A_{23} = A_{24} = A_{25} = A_{28} = A_{29} = 0 \quad (26)$$

In the following equations from Equations (27)–(30) the values of the A_{ij} (where i = 3 and j = 1, ..., 9) used in the Equation (17) are detailed.

$$A_{33} = -\left(\varepsilon_0\varepsilon'_r(r)\mu_0 r\omega^2 - \varepsilon_0\varepsilon_r(r)\mu_0\omega^2 + \beta^2\right)\left(\varepsilon_0\varepsilon_r(r)\mu_0 r\omega^2 - \beta^2 r\right)^{-1} \quad (27)$$

$$A_{36} = -\left(\varepsilon_0\varepsilon'_r(r)E_{0z} l\omega\right)\left(\varepsilon_0\varepsilon_r(r)\mu_0 H_{0z} r\omega^2 - H_{0z}\beta^2 r\right)^{-1} \quad (28)$$

$$A_{37} = \left(\varepsilon_0\varepsilon_r(r)\mu_0 r^2\omega^2 - \beta^2 r^2 - l^2\right)r^{-2} \quad (29)$$

and,

$$A_{31} = A_{32} = A_{34} = A_{35} = A_{38} = A_{39} = 0 \quad (30)$$

In the Equations (31)–(34) the value of the coefficients A_{ij} (where i = 4 and j = 1, ..., 9) which have been defined in the Equation (18), are detailed.

$$A_{44} = -\left(\varepsilon_0\varepsilon'_r(r)\mu_0 r\omega^2 - \varepsilon_0\varepsilon_r(r)\mu_0\omega^2 + \beta^2\right)\left(\varepsilon_0\varepsilon_r(r)\mu_0 r\omega^2 - \beta^2 r\right)^{-1} \quad (31)$$

$$A_{45} = \left(\varepsilon_0\varepsilon'_r(r)E_{0z} l\beta\omega\right)\left(\varepsilon_0\varepsilon_r(r)\mu_0 H_{0z} r\omega^2 - H_{0z}\beta^2 r\right)^{-1} \quad (32)$$

$$A_{48} = \left(\varepsilon_0\varepsilon_r(r)\mu_0 r^2\omega^2 - \beta^2 r^2 - l^2\right)r^{-2} \quad (33)$$

and where,

$$A_{41} = A_{42} = A_{43} = A_{46} = A_{47} = A_{49} = 0 \quad (34)$$

where x' denotes dx/dr, $\beta = \frac{2\pi\varepsilon_{reff}{}^{1/2}}{\lambda}$ and ε_{reff} is the effective permittivity parameter.

We can observe that this system of equations is not completely coupled. Equations (15) and (18) form a pair of mutually coupled equations in $e_{zR}(r)$ and $h_{zI}(r)$. The same can be said for Equations (16) and (17). Each pair of mutually coupled equations have a similar mathematical structure. Then, it is possible to reduce the problem of microwave propagation inside cylindrical wood samples with arbitrary radial relative permittivities to a pair of ordinary differential equations. We shall choose Equations (15) and (18) for convenience. The results were calculated and simplified by means of the Maxima program [26].

In order to solve the final equations, an implicit high order Runge–Kutta algorithm was used. Implicit RK algorithms are more stable than their explicit counterparts [27] and this fact eliminates some problems related with the periodic nature of the dielectric structure of wood and the extreme sensibility of the solutions to the value of the effective permittivity. Although the core equations of this problem are the same as the equations for a Bragg fiber in our previous work [24], there are important conceptual and computational differences between both problems. First of all, the relative permittivities of adjacent layers in the wood model are larger than in a Bragg fiber and conductivity is not present in optical fibers. More important even is the consideration of the grain angle in the wood model which introduces new complexities and new propagation modes. This grain angle would be similar to a Bragg fiber with torsion, which was not considered in our previous work. Also, the ratio between the wavelength and the dimensions of the rings is different, producing subtle effects that have forced us to develop a new numerical approach to solve the final equations. While in our previous calculations, collocation methods were successfully used, in this case an implicit, unconditionally stable, RK algorithm has been developed in order to avoid large numerical instabilities produced by the mode splitting introduced by the grain angle dependence on the relative permittivity.

2.2. Numerical Simulation

Due to mathematical constraints, conductivity cannot be easily introduced in the exact model, because the Maxwell equations cannot be decoupled. Therefore, a detailed numerical simulation of an idealized cylindrical sample of wood has been performed in order to study the effect of moisture on microwave propagation. The commercial software CST Microwave Studio® [22], which implements a finite-integral technique (FIT) approach, was used.

The sample was formed by concentrically layers of two different permittivities corresponding to typical epsilon values of poplar [27] using the dielectric Cartesian tensor facility of CST (Computer Simulation Technology). The exact values are shown in Figure 1. Summer and spring rings are independently considered. Experimental dielectric and conductivity data for both dry and wet wood were obtained from [28–31]. The thickness of growth rings inside poplar has been taken from pictures of several samples from the Madrid area and a rounded mean value has been used for the simulations. Thus, this study must be considered as a general description of microwave propagation inside an actual ring structured wood but not a detailed analysis of a particular wood sample.

The selected frequency for our study has been 3 GHz for numerical convenience in the case of the semianalytical calculations. The permittivity values can be considered almost unaltered from the more common 2.45 GHz according to [27]. However, according to the electric field distribution shown in Figures 2 and 3 for dry and wet poplar sample, the effect of the microwave frequency is noticeable in spite of the constant value of the permittivity at those frequencies. An important consequence of these results is the requirement of several frequencies to achieve a more homogenous electric field distribution inside wood.

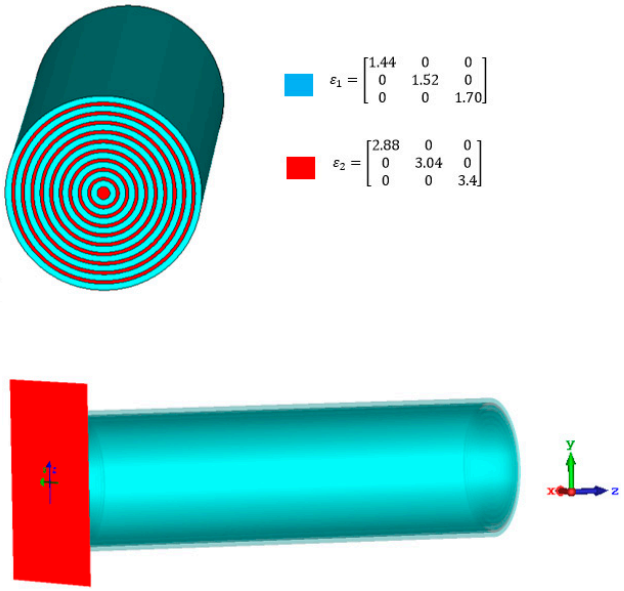

Figure 1. Structural configuration of dielectric tensors and excitation used for CST (Computer Simulation Technology) analysis.

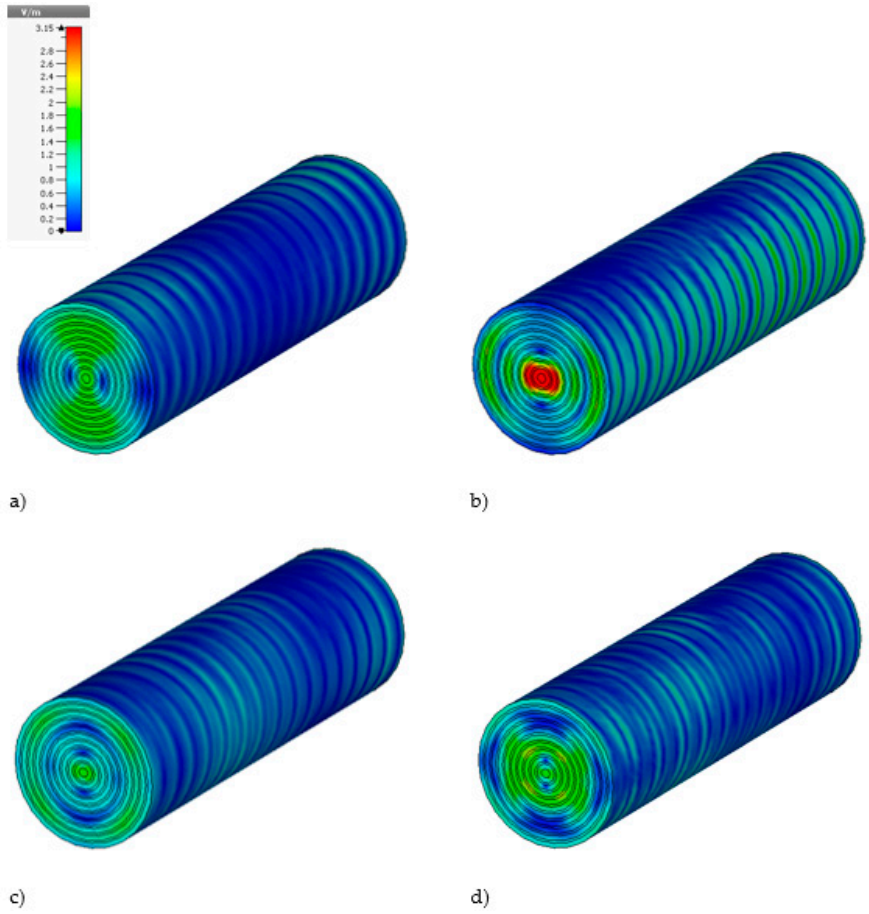

Figure 2. Electric field distribution inside dry poplar. (**a**) f = 2.45 GHz 50% permittivity variation; (**b**) f = 3 GHz 50% permittivity variation; (**c**) f = 2.45 GHz 100% permittivity variation; and (**d**) f = 3 GHz 100% permittivity variation.

A limitation of our study is that real wood has different growth ring thicknesses, heterogeneous zones with defects, moisture gradients, gaps, etc., which could be introduced in future studies.

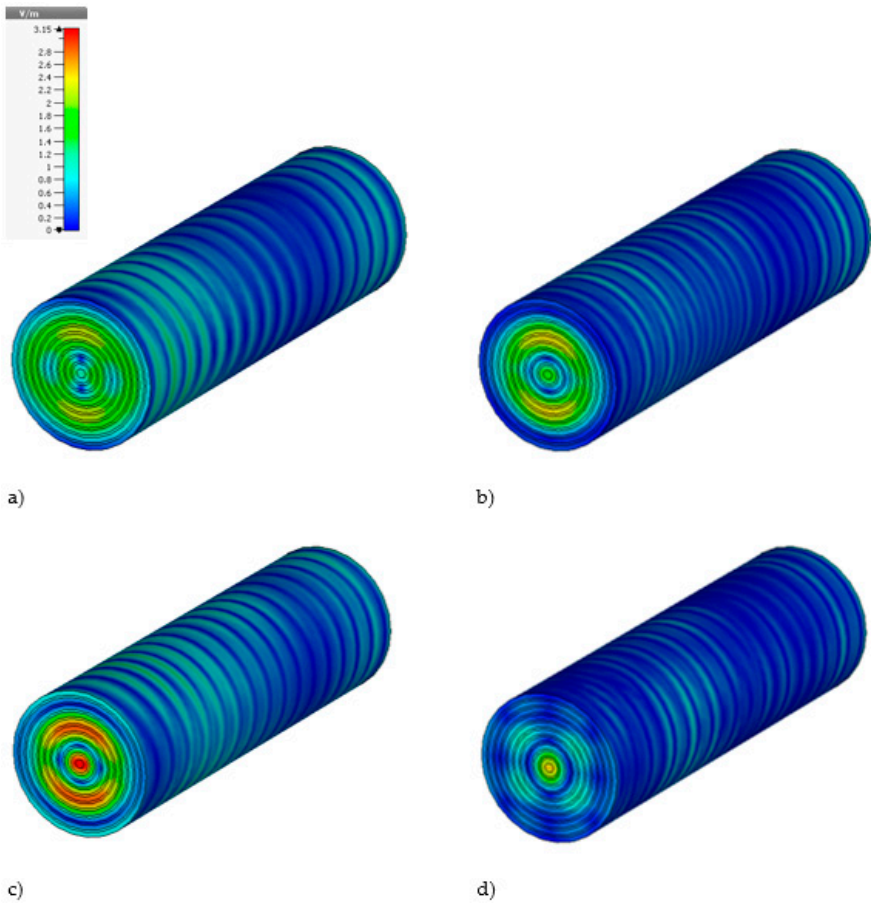

Figure 3. Electric field distribution inside wet poplar. (**a**) f = 2.45 GHz 50% permittivity variation; (**b**) f = 3 GHz 50% permittivity variation; (**c**) f = 2.45 GHz 100% permittivity variation; and (**d**) f = 3 GHz 100% permittivity variation.

3. Results and Discussion

In both models, analytical and numerical, axial excitation and propagation of microwaves are studied. The timber is excited by an incident plane wave along the z-axis, the electric field is perpendicular to the cylinder axis, and so the magnetic field, as shown in Figure 1. The relative permittivity function used for the semianalytical analysis is shown in Figure 4. The semianalytical model shows a slow modulation of the amplitude of the electric field due to the periodic nature of the dielectric layers of wood, as can be seen in Figures 5 and 6. The behavior of this permittivity function is modelled on [28]. For simplicity and easier convergence of the RK algorithm, uniform growth ring thickness and a lower variation between different wood dielectric values in the radial direction was used. This is clearly a limitation of the semianalytical model and one of the main reasons for using also a full numerical simulation tool. Thus, the results are not exactly the same as the ones calculated using experimental poplar data.

For the previous reasons, the semianalytical method is restricted to only 5 rings, while the full numerical simulations range from 5 growth rings to 20. The thickness of growth rings are taken form [27]. The semianalytical results can be seen as a validation technique for this study. The length of the sample is 1 m in both methods. The semianalytical and numerical simulations have been done at 3 GHz because the wavelength at that frequency is comparable to the diameter of the wood sample.

Moreover, that frequency is similar to the value which is employed in commercial microwave drying ovens [32,33].

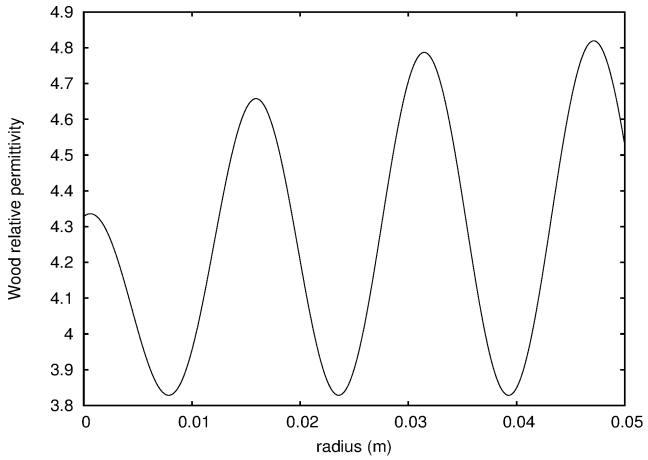

Figure 4. Relative permittivity function used for the calculation of the electric field in the exact model.

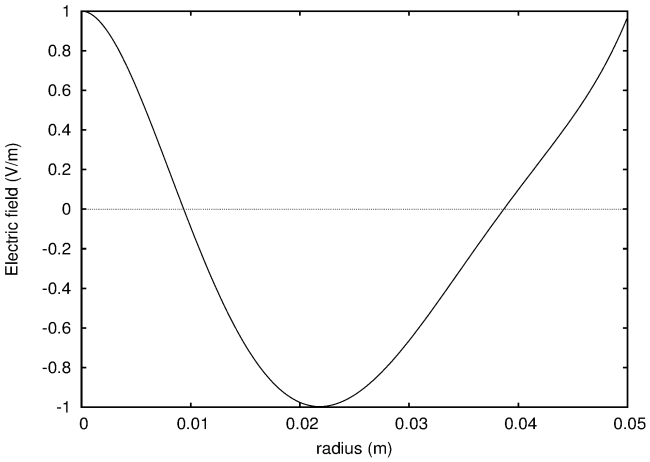

Figure 5. Particular solution with analytical analysis of the electric field inside a cylindrical wood sample when the corrective factor for the effective relative permittivity is 0.70 and the grain angle is $\alpha = 45°$.

The periodic structure produces the modification of the values of the relative permittivity, which, in turn, modifies the electromagnetic field modes inside the wood cylinder. In order to apply microwave propagation to the detailed study of internal ring structure of wood, higher frequencies up to tens of GHz (microwaves in the mm range) are necessary. However, at such short wavelengths, the effect of limited skin depth and increased attenuation should be studied carefully. Besides, the computational demands are far higher, so this will be considered in future works. If such accuracy could be practically achieved, a non-invasive determination of tree ages would be possible, for example.

The solutions are valid only for certain values of the effective relative permittivity (permittivity eigenvalues) due to the existence of discrete propagation modes inside the cylindrical material. These eigenvalues are calculated by means of an iterative procedure which runs the RK algorithm searching for the correct behavior of the solutions. In this case, the azimuthal number of the selected propagation mode is $l = 1$. Therefore, every mode is characterized by a definite value of the effective relative permittivity, which can be expressed as a correction factor multiplying the mean effective relative permittivity.

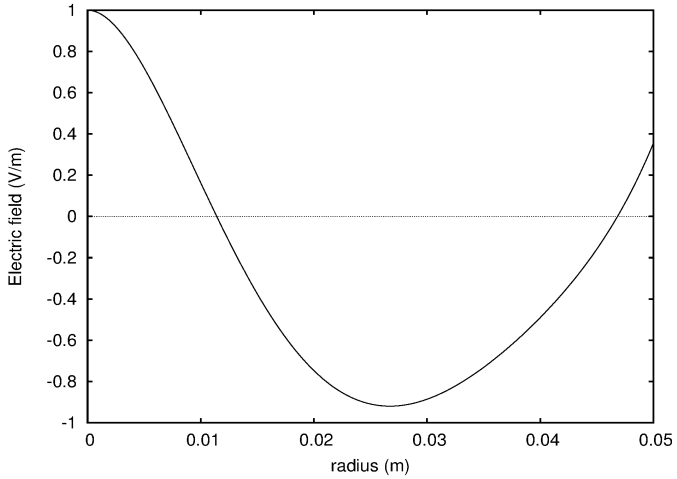

Figure 6. A particular solution with analytical analysis of the electric field inside a cylindrical wood sample when the corrective factor for the effective relative permittivity is 0.66 and the grain angle is $\alpha = 30°$.

The exact model allows the variation of the grain angle, α. The grain angle is defined as the angle between the timber axis and the wood logs. It is the longitudinal arrangement of wood timbers or the pattern resulting from this. From an analytical perspective, if the grain angle had been inserted directly in the cylindrical Maxwell's equations, they would not be separable. In fact, helicoidal coordinates should be used, but the model was too complex for the present study. Instead of a full helicoidal model, we have made the hypothesis that the effect of the grain angle can be considered using only its variation inside the dielectric permittivity profile.

The numerical simulation of the grain angle would imply a helicoidally arrangement of different wood elements, so that parametric functions should be used inside the Cartesian dielectric tensor of the CST software. In this regard, the analytical model is more general, although conductivity effects are hard to introduce, if additional hypotheses are not made. Due to the limitations of both approaches, we have opted for a combined study, comparing the results for a neutral grain angle and dry wood. Then, the effect of moisture is studied using numerical analysis and the grain angle variation uses the analytical model.

In Figures 5 and 6, we can compare the results for $\alpha = 45°$ and $30°$, respectively. It must be noted that the correction factor for the effective relative permittivity changes with the value of the grain angle, so that the corrections are 0.70 for $\alpha = 45°$ and 0.66 $\alpha = 45°$. The ability to calculate the grain angle is important, because grain angle is related with the mechanical strength of wood. The effective value of the relative permittivity due to the grain angle correction is calculated by means of an iterative bisection algorithm which finds the correct asymptotic behavior of the oscillating fields inside wood after a number of rings. These calculations are time consuming and numerically unstable, even using the implicit Runge–Kutta algorithm for the propagation step. Due to this, only two decimal figures and five rings are considered in Figures 5 and 6, while the numerical model—which discards the grain angle influence—can be calculated for a larger number of rings.

The CST simulations have been done without considering the grain angle. The numerical values for the simulations were: length = 1 m, number of cylindrical layers = from 5 to 20, radius = from 35 to 145 mm. Growth ring thickness are different depending on the season. One type has been set to 10 mm and the other to 5 mm. The values of the dielectric constant of each layer have been taken from [27] and they are shown in Figure 1.

The numerical FIT simulation allows the study of a layer of growth rings. In general, the results in Figures 7–12 prove the critical effect of the number of rings on the electric field distribution inside of poplar wood. Besides, this effect is not trivial according to the radial electric field variation seen in Figures 13–18. The electric field maxima varies with the number of the growth rings both, in the

radial and longitudinal directions. A direct consequence of these results for heating applications is that the thermal distribution inside wood would vary critically from one sample to another with different thicknesses. For the calculations, two extreme cases of the permittivity variation between growth rings (50% and 100%), according to the literature [28], have been studied. Comparing Figure 7, Figure 9, and Figure 11 (50% dielectric variation) with Figures 8, 10 and 12 (100% dielectric variation) it can be concluded that the effect of this variable is very important. For example, in Figures 7 and 8 it can be observed that the most remarkable changes in the electric field distribution, are produced between the 5-ring samples and the 15-ring samples, in both, the radial and the axial direction. This implies that, even if two poplar samples have the same dimensions, their electric and thermal behavior can be completed different.

In Figures 9–12 the influence of moisture on the distribution of the electric field inside poplar wood is explored. According to these results, there are two main conclusions of this: the electric field distribution is completely altered by the presence of moisture and the number of rings changes this behavior in a non-predictable way. For example, in the five rings case, moisture produces a noticeable central focusing effect making the wood sample similar to a metallic waveguide. On the contrary, the 10-ring case shows a completely opposite behavior, from a central distribution in the dry case to a much attenuated radial distribution. The axial distribution is also noticeably altered. The implications for heating applications are clear.

A detailed study of the radial electric field distribution is shown in Figures 13–18. In this set of figures, the combined and complex interaction among the analyzed variables are more clearly seen. The maximum of the electric field is displaced from the center to a different position depending on the number of the growth rings. Also, the shape of the electric field distribution is greatly affected.

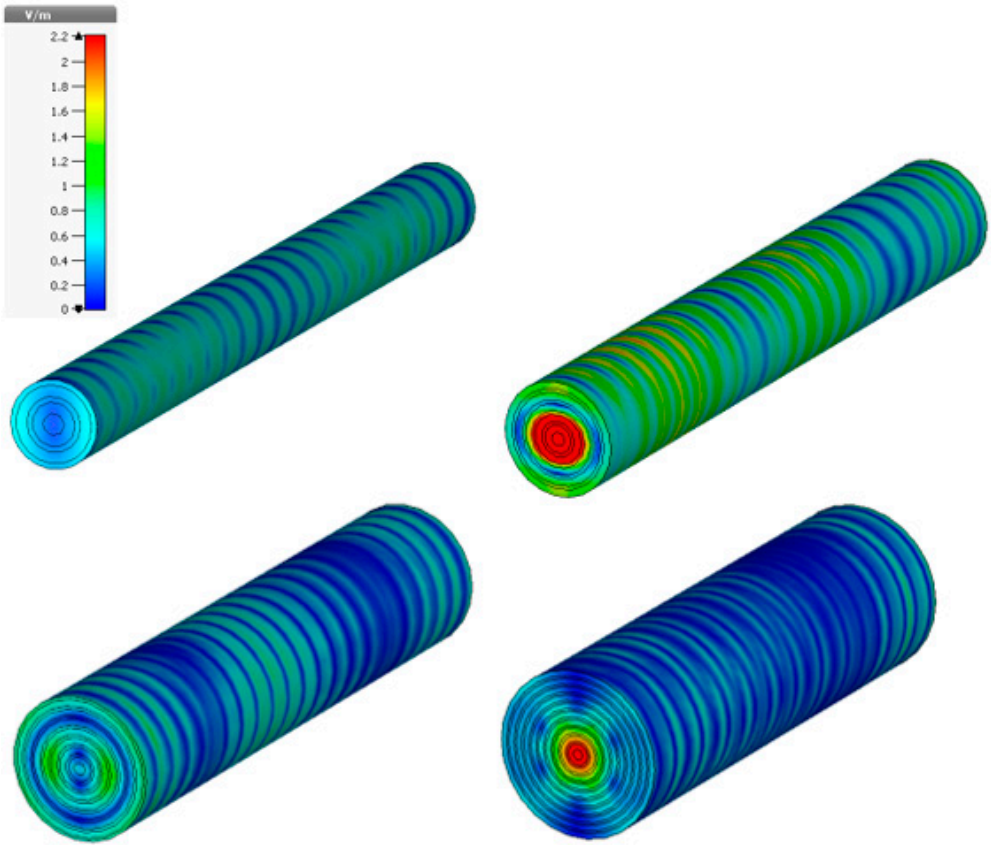

Figure 7. Electric field distribution inside dry poplar wood with different values of the number of growth rings with 50% permittivity variation at 3 GHz.

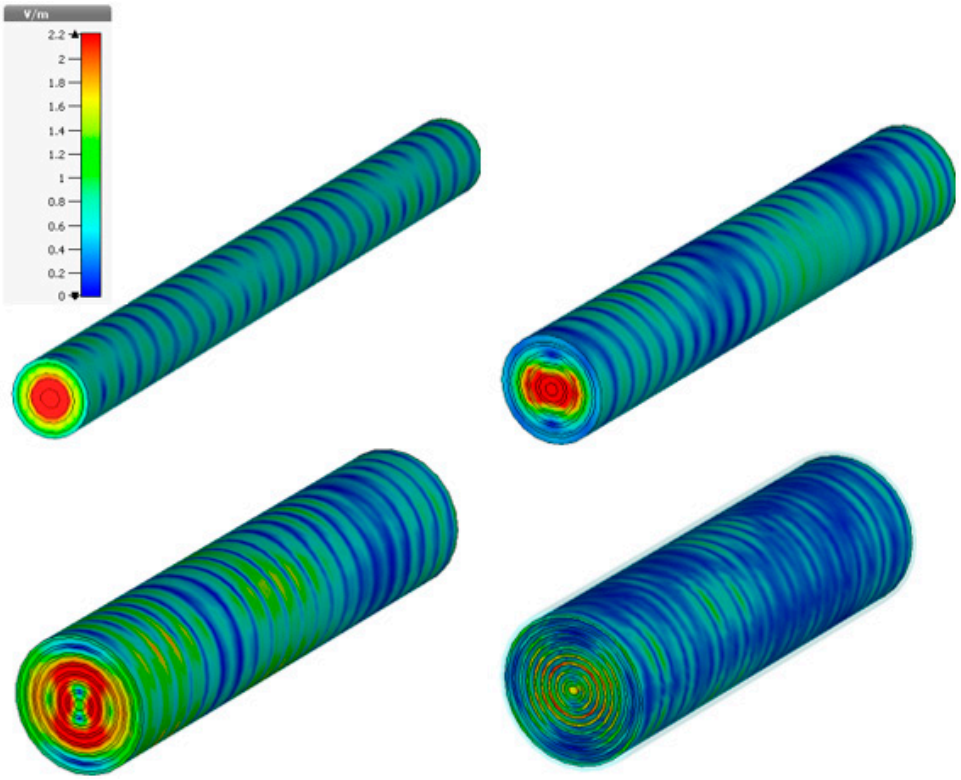

Figure 8. Electric field distribution inside dry poplar wood with different values of the number of growth rings with 100% permittivity variation at 3 GHz.

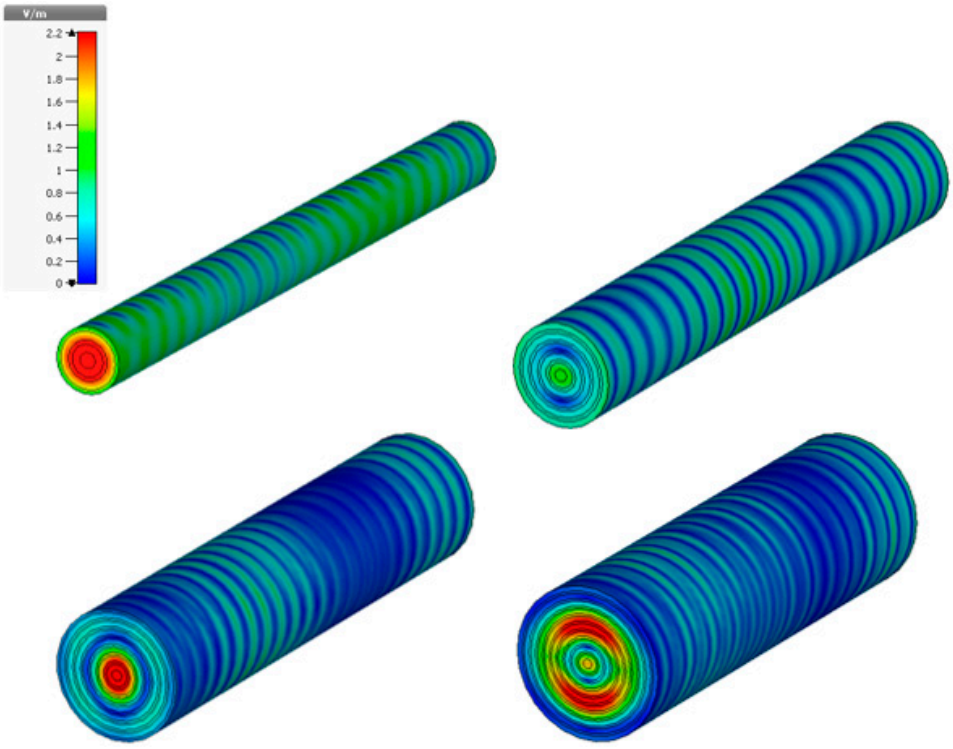

Figure 9. Electric field distribution inside wet poplar wood with different values of the number of growth rings with 50% permittivity variation at 3 GHz. The dielectric constant values considered are the same as the Figure 7.

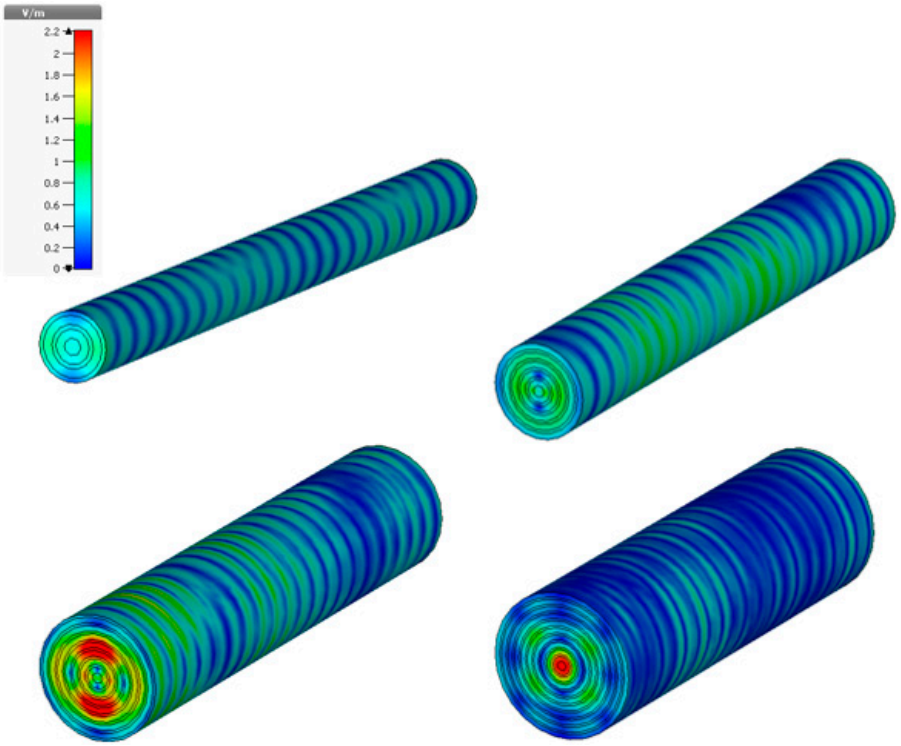

Figure 10. Electric field distribution inside wet poplar wood with different values of the number of growth rings with 100% permittivity variation at 3 GHz. The dielectric constant values considered are the same as the Figure 8.

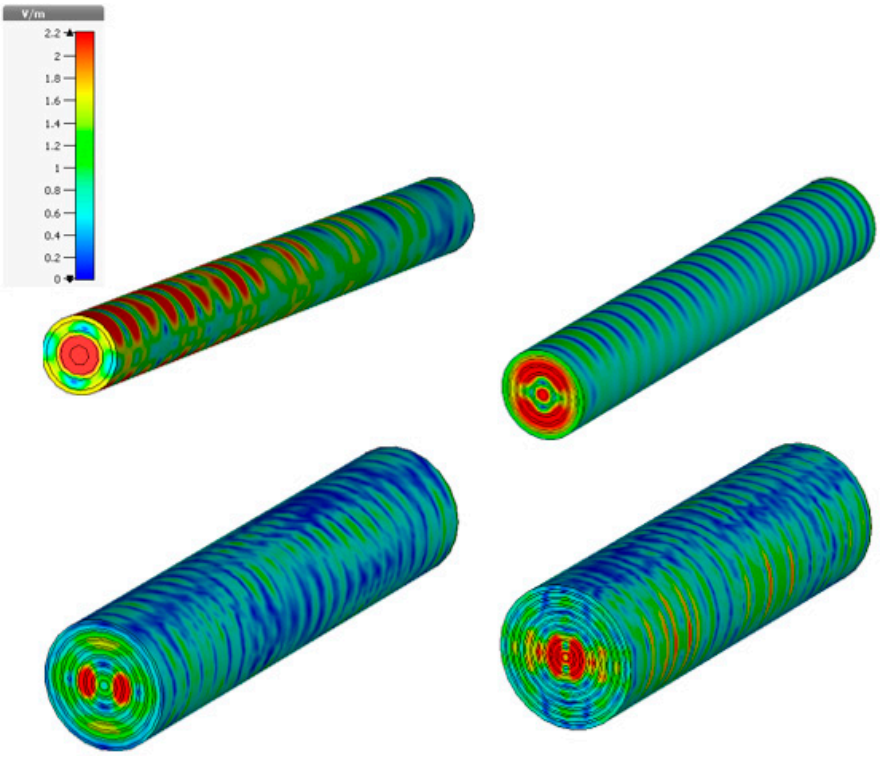

Figure 11. Electric field distribution inside wet poplar wood with different values of the numbers of growth rings with 50% permittivity variation at 3 GHz. Dielectric constant values were used with 28% moisture content according to [27].

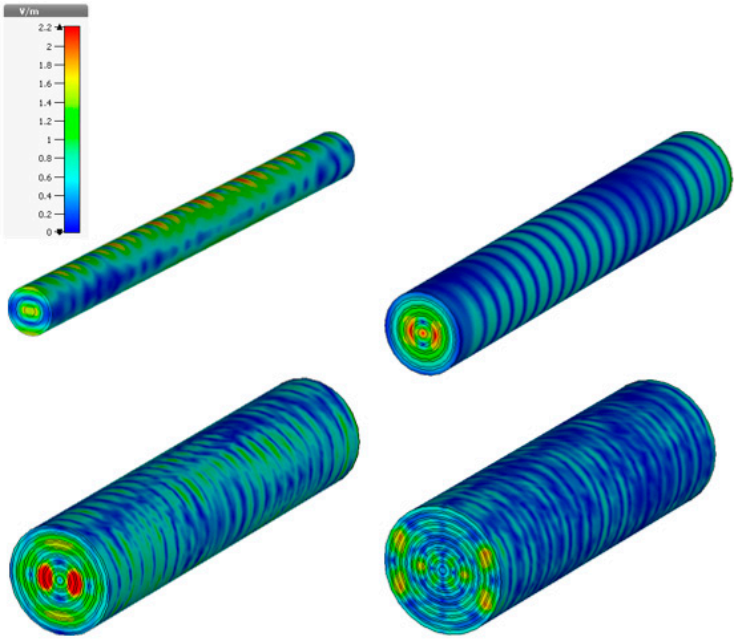

Figure 12. Electric field distribution inside wet poplar wood with different values of the number of growth rings with 100% permittivity variation at 3 GHz. Dielectric constant values were used with 28% moisture content according to [27].

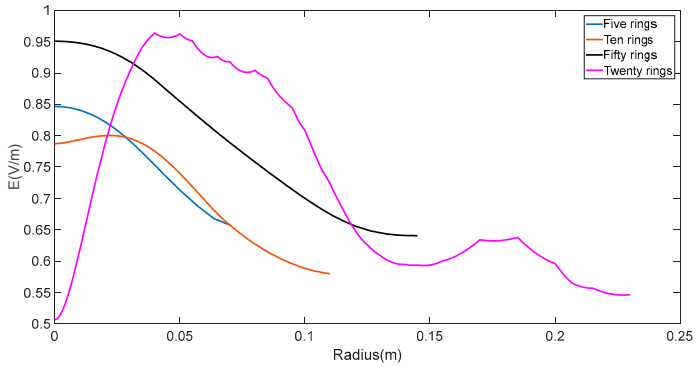

Figure 13. Radial profile of the electric field for a dry poplar sample with a 50% dielectric constant variation between growth rings.

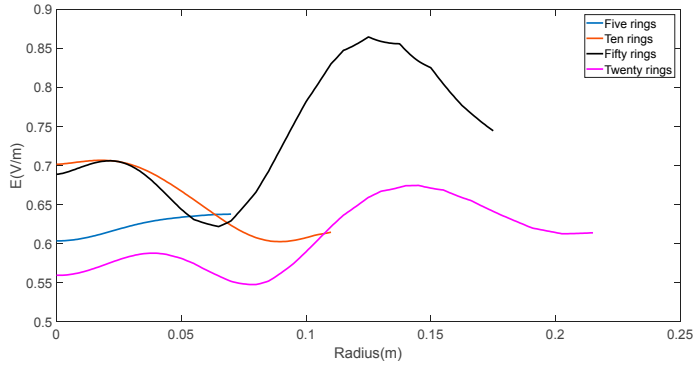

Figure 14. Radial profile of the electric field for a dry poplar sample with a 100% dielectric constant variation between growth rings.

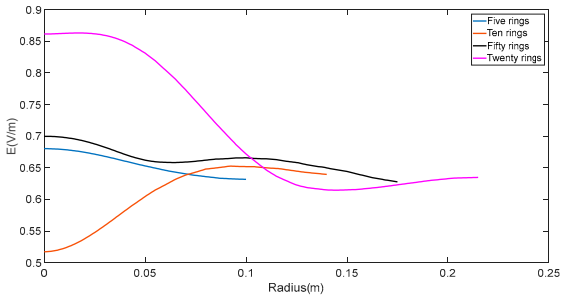

Figure 15. Radial profile of the electric field for a wet poplar sample with a 50% dielectric constant variation between growth rings. Dielectric constant values were used with 0% moisture content according to [27].

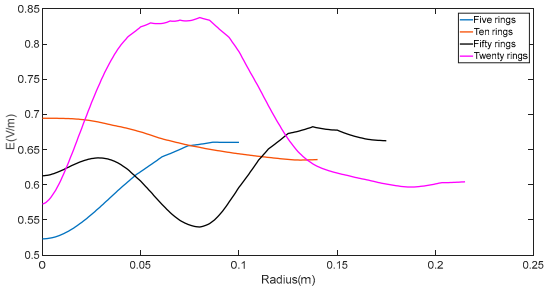

Figure 16. Radial profile of the electric field for a wet poplar sample with a 100% dielectric constant variation between growth rings. Dielectric constant values were used with 0% moisture content according to [27].

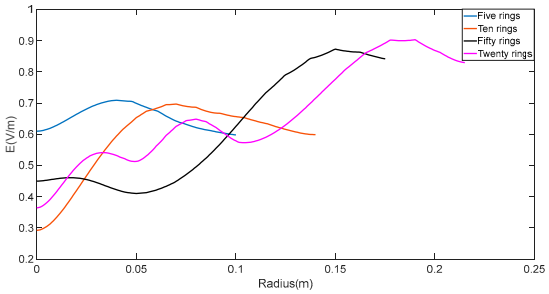

Figure 17. Radial profile of the electric field for a wet poplar sample with a 50% dielectric constant variation between growth rings. Dielectric constant values were used with 28% moisture content according to [27].

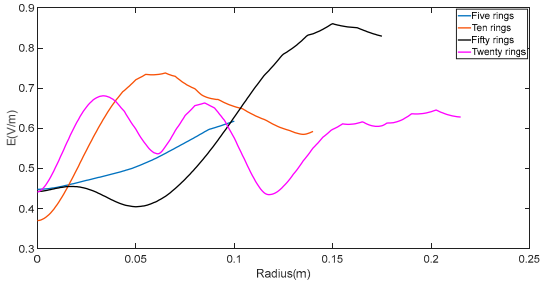

Figure 18. Radial profile of the electric field for a wet poplar sample with a 100% dielectric constant variation between growth rings. Dielectric constant values were used with 28% moisture content according to [27].

4. Conclusions

Semianalytical and numerical models of microwave propagation in wood have been performed. The electromagnetic field distribution inside cylindrical wood is a complex phenomenon due to its quasiperiodic ring structure. Both the number of growth rings and moisture content modify the microwave behavior in complex and unexpected ways. The effects of grain angle and moisture have also been considered, using two complementary approaches, semianalytical, and numerical. Grain angle affects the value of the effective permittivity of wood and influences the radial distribution of the electric field inside wood, changing the radial position of the electric field maximum slowly. More critically, moisture completely alters both the radial and axial behavior of microwave propagation inside poplar wood. Depending on the numbers of the growth rings, a cylindrical sample of poplar wood performs like a metallic waveguide. The implications of these results for many applications of microwaves for wood treatment and testing are clear. For example, optimization of heating wood in microwave ovens would be a much more complex process than intuitively expected. Moreover, for nondestructive in situ testing purposes, the interpretation of data could be greatly affected by these heterogeneous focusing phenomena.

Our study is limited by several factors. Semianalytical calculations are very complex and numerically demanding in the end, so they do not present many advantages over the numerical ones, except for theoretical insight. The semianalytical method cannot address the effect of moisture, but can study the grain angle. On the contrary, numerical simulations have no problem with water content, but implementing helicoidally variations of the permittivity is complex. It is expected that these results can be qualitatively and tentatively extrapolated to many species of wood, but in this work, the calculated and simulated values correspond to poplar samples.

Acknowledgments: This work has been funded by the Spanish Ministry of Economy, Industry and Competitiveness research project with reference AGL2013-44631-P.

Author Contributions: R.S.-M. and J.A.M.-R. conceived and designed the experiments. R.S.-M., P.-L.L.-E. and J.A.M.-R. performed the simulations. R.S.-M., J.A.-H. and C.A.-C. analyzed the data and results. R.S.-M., P.-L.L.-E., J.A.M.-R., J.A.-H. and C.A.-C. wrote and corrected the paper.

Conflicts of Interest: The authors declare no conflict of interest.

References

1. Bogosanovic, M.; Al Anbuky, A.; Emms, G.W. Overview and comparison of microwave noncontact wood measurement techniques. *J. Wood Sci.* **2010**, *56*, 357–365. [CrossRef]
2. Lazarescu, C.; Avramidis, S. Heating characteristics of western hemlock (*Tsuga Heterophylla*) in a high frequency field. *Eur. J. Wood Wood Prod.* **2012**, *70*, 489–496. [CrossRef]
3. Gilbert, A.F.; Cooper, D.F. A model for thawing frozen wood using microwave energy. *J. Pulp Paper Sci.* **2001**, *27*, 34–40.
4. Nioua, Y.; El Bouazzaoui, S.; Achour, M.E.; Costa, L.C. Modeling microwave dielectric properties of polymer composites using the interphase approach. *J. Electromagn. Waves Appl.* **2017**, *31*, 1343–1352. [CrossRef]
5. Krraoui, H.; Mejri, F.; Aguili, T. Dielectric constant measurement of materials by a microwave technique: Application to the characterization of vegetation leaves. *J. Electromagn. Waves Appl.* **2016**, *30*, 1643–1660. [CrossRef]
6. Krraoui, H.; Mejri, F.; Aguili, T. Electromagnetic diffraction modeling of the finite multi-dielectric thickness in metallic wave-guides using GEC method: Application to the characterization of vegetation leaves. *J. Electromagn. Waves Appl.* **2016**, *30*, 985–1004. [CrossRef]
7. Martin, P.; Collet, R.; Barthelemy, P.; Roussy, G. Evaluation of wood characteristics: Internal scanning of the material by microwaves. *Wood Sci. Technol.* **1987**, *21*, 361–371. [CrossRef]
8. Goy, B.; Martin, P.; Leban, J.M. The measurement of wood density by microwave sensor. *Holz. Als. Roh-Und. Werkstoff* **1992**, *50*, 163–166. [CrossRef]
9. Shen, J.; Schajer, G.; Parker, R. Theory and practice in measuring wood grain angle using microwaves. *IEEE Trans. Instrum. Meas.* **1994**, *43*, 803–809. [CrossRef]

10. Johansson, J.; Hagman, O.; Fjellner, B.A. Predicting moisture content and density distribution of Scots pine by microwave scanning of sawn timber. *J. Wood Sci.* **2003**, *49*, 312–316. [CrossRef]
11. Schinker, M.G.; Hansen, N.; Spiecker, H. High-frequency densitometry-a new method for the rapid evaluation of wood density variations. *IAWA J.* **2003**, *24*, 231–239. [CrossRef]
12. Lundgren, N.; Hagman, O.; Johansson, J. Predicting moisture content and density distribution of Scots pine by microwave scanning of sawn timber II: Evaluation of models generated on a pixel level. *J. Wood Sci.* **2006**, *52*, 39–43. [CrossRef]
13. Schajer, G.S.; Orhan, F.B. Measurement of wood grain angle, moisture content and density using microwaves. *Eur. J. Wood Wood Prod.* **2006**, *64*, 483–490. [CrossRef]
14. Voichita, B. Nondestructive Characterization and Imagining of Wood. In *Springer Series in Wood Science*; Springer: Berlin, Germany, 2003, ISBN 978-3-662-08986-6.
15. Glay, D.; Lasri, T.; Mamouri, A. Nondestructive Permittivity Profile Retrieval of Non-Planar Objects by Free Space Microwave Techniques. *Subsurf. Sens. Technol. Appl.* **2001**, *2*, 391–409. [CrossRef]
16. Sjödén, T.; Nilsson, B.; Nordebo, S. Numerical verification of a microwave impedance model for a twisted wooden cylinder. *AIP Conf. Proc.* **2008**, *1106*, 243–249. [CrossRef]
17. Jaskowska-Lemańska, J.; Wałach, D. Impact of the Direction of Non-destructive Test with Respect to the Annual Growth Rings of Pine Wood. *Procedia Eng.* **2016**, *161*, 925–930. [CrossRef]
18. Tan, E.L. Cylindrical vector wave function representations of the dyadic Green's functions for cylindrical multilayered gyrotropic bianisotropic media. *Prog. Electromagn. Res.* **2000**, *26*, 199–222. [CrossRef]
19. Li, L.W.; Yeap, S.B.; Leong, M.S.; Yeo, T.S.; Kooi, P.S. Eigenfunctional representation of dyadic Green's functions in cylindrically multilayered gyroelectric chiral media. *Prog. Electromagn. Res.* **2003**, *42*, 143–171. [CrossRef]
20. Zhang, W. Two-dimensional microwave tomographic algorithm for radar imaging through multilayered media. *Prog. Electromagn. Res.* **2014**, *144*, 261–270. [CrossRef]
21. Martinez-Rojas, J.A.; Alpuente-Hermosilla, J.; Piñeiro, J.; Sanchez-Montero, R. Rigorous full vectorial analysis of electromagnetic wave propagation in 1D. *Prog. Electromagn. Res.* **2006**, *63*, 89–105. [CrossRef]
22. Manual of CST MICROWAVE STUDIO. Available online: https://www.cst.com/products/CSTMWS (accessed on 12 December 2017).
23. Hansson, L.; Lundgren, N.; Antti, A.L.; Hagman, O. Finite element modeling (FEM) simulation of interactions between wood and microwaves. *J. Wood Sci.* **2006**, *52*, 406–410. [CrossRef]
24. Rojas, J.A.M.; Alpuente, J.; Lopez, P.; Sanchez, R. Study of leaky modes in high contrast Bragg fibres. *J. Opt. A Pure Appl. Opt.* **2007**, *9*, 833–837. [CrossRef]
25. Manual of Maxima. Available online: http://maxima.sourceforge.net/ (accessed on 15 December 2017).
26. Burrage, K.; Butcher, J.C. Stability criteria for implicit Runge–Kutta methods. *SIAM J. Numer. Anal.* **1979**, *16*, 46–57. [CrossRef]
27. Sahin, H.; Ay, N. Dielectric properties of hardwood species at microwave frequencies. *J. Wood Sci.* **2004**, *50*, 375–380. [CrossRef]
28. Torgovnikov, G. Dielectric Properties of Wood and Wood-Based Materials. In *Springer Science and Business Media*; Springer: Berlin, Germany, 1993, ISBN 978-3-642-77453-9.
29. Peyskens, E.; De Pourcq, M.; Stevens, M.; Schalck, J. Dielectric properties of softwood species at microwave frequencies. *Wood Sci. Technol.* **1984**, *18*, 267–280. [CrossRef]
30. Daian, G.; Taube, A.; Birnboim, A.; Shramkov, Y.; Daian, M. Measuring the dielectric properties of wood at microwave frequencies. *Wood Sci. Technol.* **2005**, *39*, 215–223. [CrossRef]
31. Daian, G.; Taube, A.; Birnboim, A.; Daian, M.; Shramkov, Y. Modelling the dielectric properties of wood. *Wood Sci. Technol.* **2006**, *40*, 237–246. [CrossRef]
32. McConnell, D.R. Energy consumption: A comparison between the microwave oven and the conventional electric range. *J. Microw. Power* **1974**, *9*, 341–347. [CrossRef]
33. Vollmer, M. Physics of the microwave oven. *Phys. Educ.* **2004**, *39*, 74. [CrossRef]